Mesoscopic Transport of Quantum Anomalous Hall Effect in the Submicron Size Regime

Gang Qiu[®], ^{1,*} Peng Zhang[®], ¹ Peng Deng[®], ¹ Su Kong Chong, ¹ Lixuan Tai, ¹
Christopher Eckberg[®], ^{2,3,4} and Kang L. Wang^{1,5,†}

¹Department of Electrical and Computer Engineering, University of California Los Angeles,
Los Angeles, California 90095, USA

²Fibertek Inc., Herndon, Virginia 20171, USA

³DEVCOM Army Research Laboratory, Adelphi, Maryland 20783, USA

⁴DEVCOM Army Research Laboratory, Playa Vista, California 90094, USA

⁵Department of Physics and Astronomy, University of California Los Angeles, Los Angeles, California 90095, USA

(Received 15 December 2021; accepted 9 May 2022; published 27 May 2022)

The quantum anomalous Hall (QAH) effect has been demonstrated in two-dimensional topological insulator systems incorporated with ferromagnetism. However, a comprehensive understanding of mesoscopic transport in submicron QAH devices has not yet been established. Here we fabricated miniaturized QAH devices with channel widths down to 600 nm, where the QAH features are still preserved. A backscattering channel is formed in narrow QAH devices through percolative hopping between 2D compressible puddles. Large resistance fluctuations are observed in narrow devices near the coercive field, which is associated with collective interference between intersecting paths along domain walls when the device geometry is smaller than the phase coherence length L_{ϕ} . Through measurement of size-dependent breakdown current, we confirmed that the chiral edge states are confined at the physical boundary with its width on the order of Fermi wavelength.

DOI: 10.1103/PhysRevLett.128.217704

Introduction.—The quantum anomalous Hall (QAH) effect arises when long-range ferromagnetic order is introduced into a topological insulator two-dimensional (2D) film, which opens an exchange gap on the surface, and chiral edge states are formed due to broken time-reversal symmetry. These topologically protected chiral edge states are immune to backscattering and thus can support dissipationless current flow in the longitudinal direction, whereas the Hall resistance is quantized into h/e^2 . Experimentally, the OAH effect was first demonstrated by introducing properly engineered transition metal magnetic dopants (Cr or V) into topological insulator thin films [1-4]. Recently, the QAH effect has also emerged in intrinsic 2D van der Waals material-based systems, including MnBi₂Te₄ [5] and moiré patterns in twisted bilayer graphene [6] and MoTe₂/WSe₂ heterostructures [7].

Because of the zero-loss current carrying capability, QAH insulators are deemed as a promising platform to design novel quantum devices that operate at low temperatures to process quantum information [8]. When coupled with an *s*-wave superconductor, proximitized topological superconductivity can also be introduced in QAH heterostructures toward fault-tolerant quantum computing applications [9,10]. For potential scalable manufacturing of topological qubits, QAH systems have a unique advantage over quantum Hall (QH) systems, which require a large external magnetic field to drive two-dimensional electron gases (2DEGs) into Landau quantization. So far,

experimental efforts have been focusing on macroscopic QAH devices where the chiral edge modes are treated as a perfect 1D conductor at the physical boundary of the QAH mesa. In practice, a key question to be addressed is where the chiral edge states are physically located, and how wide the chiral edge channel is. Although the chiral edge states have been directly visualized through microwave scanning microscopy [11], the several micron wide conductive edge should not be interpreted as the edge channel width as it is most likely limited by the resolution of the instrumentation. In this Letter, we report a comprehensive investigation of the transport behavior in miniaturized QAH devices in the submicron size regime. A mesoscopic picture of chiral edge states is presented, which is in sharp contrast to the QH edge states. Our work assesses the geometrical size limit above which the QAH effect can survive and offers an insight for physical modeling and analysis of chiral edge modes in QAH nanodevices.

Results and discussion.—Magnetic topological insulator (MTI) films were prepared by molecular beam epitaxial (MBE) growth following previously reported recipes [12,13]. Six quintuple layers of Cr_{0.12}(Bi_{0.26}Sb_{0.62})₂Te₃ film were epitaxially deposited onto GaAs (111) substrates. The samples were first patterned into a 10-μm-wide Hall bar using photolithography, then the narrow channels were further defined with electron-beam lithography. Detailed descriptions of material preparation, device fabrication, and measurement techniques are provided in Supplemental

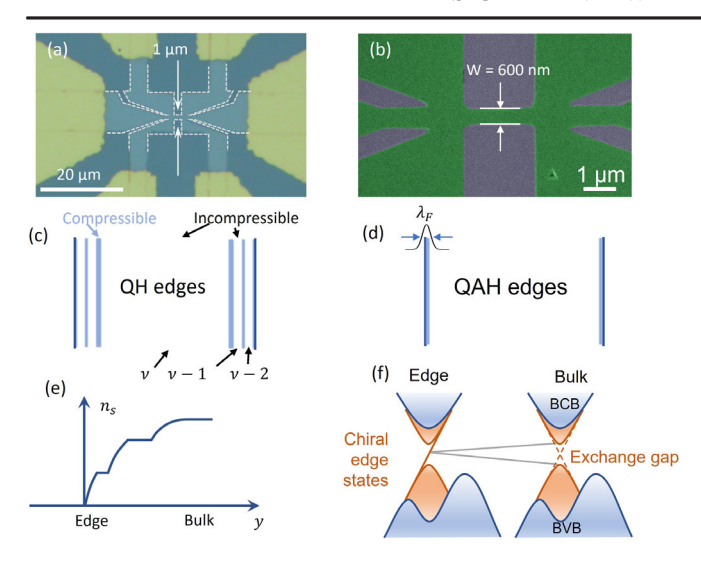


FIG. 1. Submicron size QAH devices for studying chiral edge modes. (a) An optical image of a $1-\mu$ m-wide Hall-bar device. (b) A false-colored SEM image of a $0.6-\mu$ m-wide Hall-bar device. The green region highlights the QAH film. (c) Schematics of bulk-boundary correspondence of a quantum Hall (QH) system with alternating compressible and incompressible edge states. (d) In a QAH system, edge channels are confined to the physical boundary. (e) Carrier density distributions of the QH edge to the bulk. (f) Topological band evolution from the edge to the bulk in a QAH insulator. BCB: bulk conduction band, BVB: bulk valence band.

Material Note 1 [14] along with Refs. [12,13,15]. An optical image and a false-colored scanning electron microscopy image of representative devices are shown in Figs. 1(a) and 1(b). To reveal size-dependent transport behaviors, a set of four devices was fabricated on the same MTI substrate to minimize sample-to-sample variations. The channel widths of the Hall-bar devices presented in the Letter are 5, 3, 1.5, and 0.6 μ m, respectively. Additional sets of data from a different MBE growth batch are available in Supplemental Material Note 2 and Figs. S1-S3 with a similar size-dependent trend [14]. The longitudinal resistivity ρ_{xx} and Hall resistivity ρ_{yx} of all four devices measured at 100 mK are presented in Figs. 2(a) and 2(b), respectively. To avoid the current heating effect and transverse electric field breakdown (to be discussed later), a low ac current excitation of either 0.5 or 1 nA was injected in all Hall-bar devices unless specified otherwise. Depending on the magnetization directions, ρ_{vx} is fully quantized at $\pm h/e^2$, which is originated from integer topological invariant, i.e., Chern number $C = \pm 1$ of the system. ρ_{xx} of the narrow Hall bar also resembles its macroscopic counterpart, with a vanishing ρ_{xx} when in quantized states, and a resistance peak near the coercive field H_c , corresponding to trivial insulating states during magnetic domain switching. The longitudinal conductivity σ_{xx} and transverse conductivity σ_{xy} are converted through the tensor matrix and plotted in Fig. S4 (see discussion in

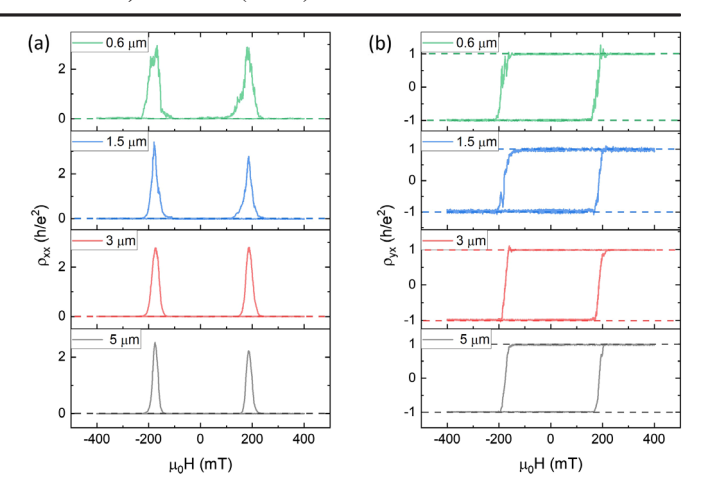


FIG. 2. Magnetic loops of submicron QAH devices with various sizes. (a) Longitudinal resistivity ρ_{xx} and (b) transverse resistivity ρ_{yx} in four devices with a channel width of 0.6, 1.5, 3, 5 μ m, respectively. All data are acquired at a base temperature of 100 mK.

Supplemental Material Note 3) [14], and the signatures of QAH states are again confirmed. Therefore we conclude that the general features of the QAH insulators are preserved in narrow channels down to 600 nm. The edge channel carrier distribution in QAH nanodevices are in sharp contrast to that of a QH system, despite the fact that two classes of systems share a similar topology and bulk-boundary correspondence [as illustrated in Figs. 1(c) and 1(d)]. In QH states, 2DEGs are localized under Landau quantization, and the carriers are spatially depopulated from sheet density n_s in the bulk to 0 at the physical edge [see Fig. 1(e)] across a depletion width, which is typically on the order of 1 μ m [16,17]. The chiral edge channels of QH states are spatially distributed in the y direction in the form of alternating compressible and incompressible strips within the depletion region [see Fig. 1(c)] [16,18]. Hence, 2DEG systems will deviate from quantum Hall states when the width of the channel is reduced close to the depletion width [19-21], as the innermost incompressible strips on the opposite edges start to merge and provide a backscattering channel. On the other hand, the incompressible bulk states in QAH insulators are gapped by magnetic exchange interaction and top-bottom surface hybridization; thus there are no carriers in the bulk nor a depletion region on the edge in QAH systems, as shown in Fig. 1(d). As a result, chiral edge states are tightly confined to the physical boundary of the films, with the wave function only extended by the order of Fermi wavelength [22], i.e., the de Broglie wavelength of chiral edge states near the Fermi energy [typically several nanometers; see Fig. 1(d)]. In this sense, the OAH effects are more robust against sizeinduced breakdown and can in principle survive in submicron devices. The remnant resistance in ρ_{xx} during field cooling is shown in an Arrhenius plot in Fig. 3(a).

The external magnetic field is biased at 500 mT, which is above the coercive field at the base temperature. At high

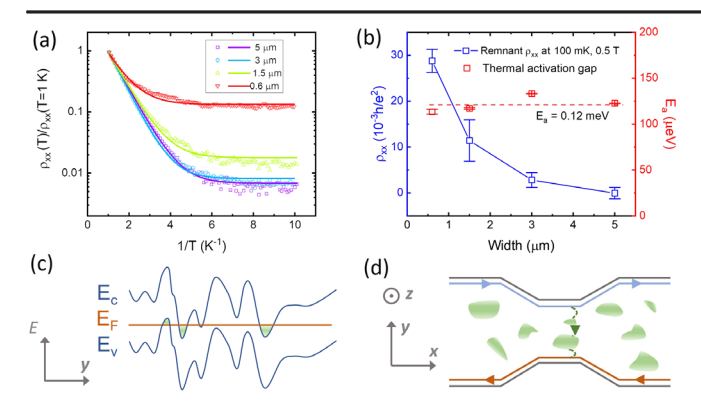


FIG. 3. Emerging backscattering channels in narrow QAH devices. (a) Normalized temperature-dependent longitudinal resistance in an Arrhenius plot. 0.5 T external magnetic field was applied during cooling. The solid lines are fitted curves from Eq. (1). (b) Remnant resistance (left-hand axis) and thermal activation gap (right-hand axis) in devices with different widths. Error bar in remnant resistance: s.d. from 20 data points. Error bar in activation gap: s.d. from curve fitting in (a). (c) Energy fluctuations along the line cut across the channel due to inhomogeneity. (d) Schematics of backscattering channels between opposite chiral edge modes by hopping through compressible 2D puddles.

temperatures, the resistance drops exponentially with 1/T at the same decaying rate for all sizes of devices, suggesting a size-insensitive bulk thermal activation gap dominates in this temperature regime. At low temperatures, the resistance saturates at a certain value, indicating a dissipative channel that originates from a temperature-independent mechanism. The activation gap can be extracted by fitting the data with the following equation:

$$\rho_{xx} = A \, \exp\left(\frac{-E_a}{k_B T}\right) + \rho_0,\tag{1}$$

where E_a is the activation energy, k_B is the Boltzmann constant, A is a device-dependent constant, and ρ_0 describes the remnant resistance contribution from backscattering processes across two edges. The average activation gap E_a is extracted to be 0.12 meV according to Eq. (1), and no obvious correlation with the geometric size can be drawn [see Fig. 3(b)]. This implies any perturbation from quantum confinement in the y direction is negligible and opposite edge channels are not hybridized. The extracted thermal activation gap is also close to the previously reported value [13]. On the other hand, ρ_0 increases monotonically with reduced sizes as plotted in Fig. 3(b). This suggests a backscattering mechanism is introduced despite topological protection when the channel width is reduced. Since the width of the narrowest device is still considerably larger than the Fermi wavelength, the direct overlapping of wave functions of chiral edge states on the opposite boundary is unlikely. However, the electrons can still be scattered to the opposite channel through

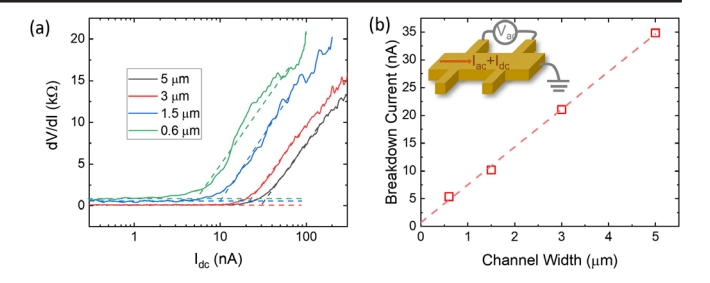


FIG. 4. Breakdown current in narrow QAH devices. (a) Differential resistance as a function of dc bias. A low ac excitation of 0.2 nA is applied. Horizontal dashed lines are the average value of resistance in the linear region, and tilted dashed lines are plotted from linear fitting over a window of over 1 decade of $I_{\rm dc}$. (b) Breakdown current versus channel width. The dashed line is the linear fitting of data. Inset: schematics of measurement setup for differential resistance.

percolative tunneling with the assistance of random compressible 2D puddles in the energy landscape [as shown in Figs. 3(c) and 3(d)]. The average 2D puddle size is estimated to be on the order of tens of nanometers following the analytic model proposed by Skinner [23] (see discussion in Supplemental Material Note 4 [14]). According to the Landauer formula, the conductance of a general quasi-1D system is related to the reflection coefficient R in the form of [24]

$$\sigma_{xx} = \frac{e^2}{h} \frac{R}{1 - R}.\tag{2}$$

From the remnant resistance, we can estimate a reflection coefficient R of 0.21% for the 0.6- μ m-wide device and 0.01% for the 5- μ m-wide device due to cross channel backscattering. This can be explained by the finite-size percolation theory, where the self-similar renormalization transformation no longer holds when the size of the system is smaller than the correlation length. In this case, when approaching the quantum critical point from the subcritical phase, the probability of forming a percolating path will increase with decreasing sizes. This is reflected in the observation that the backscattering is enhanced in narrower samples.

The size-dependent QAH critical current was also measured with a differential resistance technique. A large dc bias was sent through the device along with a small ac excitation down to 0.2 nA. Differential resistance was measured by a synchronized lock-in amplifier in the configuration illustrated in the inset of Fig. 4(b). All four devices show similar quantitative behavior [see Fig. 4(a)]. At low dc bias, the devices operate in a linear region where the remnant resistance is irrelevant to $I_{\rm dc}$ but only determined by the previously mentioned backscattering mechanism. Note that all the other data throughout the paper were acquired under either 0.5 or 1 nA ac excitation, which falls into this linear region. Above breakdown current $I_{\rm bd}$, the

resistance begins to shoot up, as large current drives the system out of QAH states, which is attributed to the electric-field-driven breakdown in the y direction [25]. The breakdown current for all devices is extracted in Fig. 4(b), and it scales linearly with the channel width. This supports the argument of electric-field-driven breakdown of QAH [25], according to the equation:

$$I_{x,\text{bd}}\frac{h}{e^2} = E_{y,\text{bd}}(W - 2\lambda_F). \tag{3}$$

Here, $I_{x,bd}$ is the breakdown current in the x direction, $E_{y,bd}$ is the QAH breakdown field in the y direction, W is the width of the channel, and λ_F is the Fermi wavelength of the chiral edge modes. We use reduced channel width $W - 2\lambda_E$ instead of W, since the breakdown current should be proportional to the incompressible bulk region width. It has been demonstrated in quantum Hall states that the Hall voltage profile in the y direction only drops in the incompressible bulk insulators, whereas the metallic edge channel has little voltage drop [26,27]. The fact that the linear relationship between the breakdown current and the channel width extrapolates to near 0 on the x axis [see Fig. 4(b)] implies that the incompressible bulk states almost extend to the entire channel and the width of chiral edge states is negligible even compared to the narrowest channel. This confirms our previous argument that the chiral edge states in QAH only reside in close vicinity of the physical edge. However, since the narrowest device in our experiment is still significantly larger compared to the predicted Fermi wavelength of chiral edge states [22], we cannot definitively attribute the origin of confinement to Fermi wavelength at this stage.

Another prominent feature in narrow devices is the resistance fluctuations near the coercive field, which is associated with multidomain behavior during topological phase transition. The resistance fluctuations $\Delta \rho_{xx}$ were extracted by removing a smooth background generated with a Savitzky-Golay filter over a window of 50 mT as shown in Fig. 5(a). One immediately notices the resistance fluctuations during magnetic switching are more pronounced in narrower devices [see Fig. 5(b)]. Similar resistance fluctuations were also observed in narrow-channel QH devices during plateau-to-plateau transitions [28–32]. The fluctuations are suppressed at elevated temperatures as shown in Fig. 5(c), confirming that this is an mesoscopic transport behavior at low temperatures rather than measurement nonidealities.

The fluctuations are quantitatively represented by the rms value of $\Delta \rho_{xx}$ within a 100 mT window around the coercive field [as highlighted in the gray area in Fig. 5(b)] and plotted for all sizes at different temperatures in Fig. 5(d). $\Delta \rho_{xx_rms}$ decays exponentially with temperature in all devices, pointing to a behavior similar to the universal conductance fluctuation phenomena that is dictated by L_{ϕ} ,

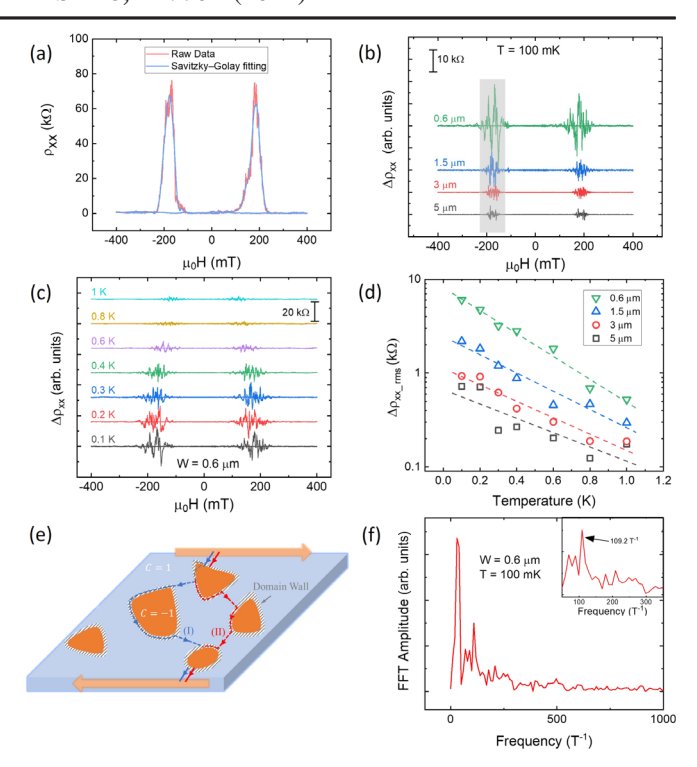


FIG. 5. Resistance fluctuations near the coercive field. (a) Extraction of resistance fluctuations by subtracting a smooth background with Savitzky-Golay filtering from raw data. (b) Size-dependent resistance fluctuations $\Delta \rho_{xx}$ measured at a base temperature of 100 mK. (c) Temperature-dependent resistance fluctuations measured in the 0.6- μ m-wide device. The data in (b) and (c) are offset for clarity. (d) Fluctuation amplitudes decay with temperature. Resistance fluctuation amplitudes are defined by the root-mean-square (rms) value of the resistance fluctuation within a 100 mT window near the coercive field, as highlighted in (b). Dashed lines are exponential decay fitting to the data. (e) Schematics of interfering paths (I) and (II) due to resonant tunneling between domains. (f) Fast Fourier transform of quasiperiod resistance fluctuation. Inset: enlarged area near the dominant frequency at 109.2 T⁻¹.

which also follows the same temperature dependence. Here we semiclassically attribute the resistance fluctuations to the electron interference effect between intersecting tunneling paths in the percolation picture during topological phase transition, as depicted in Fig. 5(e). Starting from the positive magnetic field, the MTI film is initially in $M_z = +1$ magnetization which corresponds to Chern number C = 1. When the magnetic field is swept reversely approaching the coercive field, magnetic domains start to flip into $M_z = -1$ (C = -1) domains. The domain walls between C = 1 and C = -1 give rise to trivial compressible states. Electrons on the edge states can tunnel resonantly through domain walls in multiple paths. When the size of the sample is comparable to or smaller than L_{ϕ} , the wave function of electrons in intersecting paths will interfere with each other in a similar way as the Aharanov-Bohm effect. When the sample dimension is larger than L_{ϕ} , electrons lose their phase information during scattering processes, and such fluctuations are no longer observable. Likewise, since L_{ϕ} decreases with temperature, the fluctuations drop exponentially at higher temperatures. The similar mechanism also successfully explained resistance fluctuations in narrow QH devices during plateau-to-plateau transitions [29], with a minor difference being that in QH effect electrons resonantly tunnel through extended states rather than domain walls as in the QAH cases [see Fig. 5(e)]. Since the extended states in QH films primarily arise due to lattice defects and substrate disorders, the fluctuation patterns are strongly reproducible [30], whereas the fluctuation in narrow OAH films are less reproducible because the formation of domain walls is more subject to random domain dynamics (see Supplemental Material Note 5 [14]). Finally, the quasiperiod resistance fluctuation gives a good measure of the average domain size, as whether the interference is destructive or constructive depends on the magnetic flux quanta enclosed within the intersecting paths around domains. The Fourier frequency spectrum of resistance fluctuation near the coercive field in the $W=0.6~\mu\mathrm{m}$ device is shown in Fig. 5(f). Here the first large lowfrequency peak should not be interpreted as a fluctuation frequency, as its period (~33.6 mT) is comparable to the observation window (100 mT). This peak is due to the boundary condition imposed when subtracting a smooth background. A dominant frequency associated with quasiperiod fluctuations is located at 109.2 T⁻¹, which corresponds to a quasiperiod of ~9.2 mT. This primary period ΔB can be translated into an average radius of domain size R of 280 nm following the equation:

$$\Delta B \, \pi R^2 = \Phi_0, \tag{4}$$

where Φ_0 is the magnetic flux quanta. The estimated characteristic size of superparamagnetic domain size is comparable to the value (average diameter of 175 nm at 300 mK [33]) obtained from direct imaging using scanning nano-SQUID imaging techniques [33–35].

Conclusion.—In this work, we presented a detailed study on the transport behavior of QAH insulators in the submicron size regime. QAH signatures, including vanished longitudinal resistance and quantized Hall resistance, are preserved in narrow-channel devices down to 600 nm. We argue that QAH systems are more suitable than QH systems for implementing nanoscale quantum devices since their chiral edge modes are tightly bounded to the physical boundary within the order of Fermi wavelength. We confirmed the compressible chiral edge states have negligible width by measuring width-dependent breakdown current. An emerging cross-edge backscattering channel is observed in submicron QAH devices, which is qualitatively explained by finite-size percolation theory. Resistance fluctuations near the coercive field were observed in

devices narrower than L_ϕ , which is attributed to the coherent interference between intersecting paths around emerging domain walls. The quasiperiod of the oscillations gives an estimated average domain radius of 280 nm, which matches well with the value obtained from direct imaging techniques. Our work provided a comprehensive understanding of the mesoscopic transport of the QAH effect both in quantized states and during topological phase transitions.

This work was supported by the NSF under Grants No. 1936383 and No. 2040737, the U.S. Army Research Office MURI program under Grants No. W911NF-20-2-0166 and No. W911NF-16-1-0472. C. E. is supported by Contract No. W15P7T19D0038, Delivery Order No. W911-QX-20-F-0023. The views expressed are those of the authors and do not reflect the official policy or position of the U.S. Department of Defense or the U.S. government. G. Q. would like to thank Dr. Z. Wan and Dr. Q. Qian for valuable discussions on mesoscopic transport in QH systems.

- *Corresponding author. gqiu@g.ucla.edu †Corresponding author. wang@ee.ucla.edu
- [1] C.-Z. Chang *et al.*, Experimental observation of the quantum anomalous Hall effect in a magnetic topological insulator, Science **340**, 167 (2013).
- [2] X. Kou, S.-T. Guo, Y. Fan, L. Pan, M. Lang, Y. Jiang, Q. Shao, T. Nie, K. Murata, J. Tang, Y. Wang, L. He, T.-K. Lee, W.-L. Lee, and K. L. Wang, Scale-Invariant Quantum Anomalous Hall Effect in Magnetic Topological Insulators beyond the Two-Dimensional Limit, Phys. Rev. Lett. 113, 137201 (2014).
- [3] C. Z. Chang, W. Zhao, D. Y. Kim, H. Zhang, B. A. Assaf, D. Heiman, S. C. Zhang, C. Liu, M. H. Chan, and J. S. Moodera, High-precision realization of robust quantum anomalous Hall state in a hard ferromagnetic topological insulator, Nat. Mater. 14, 473 (2015).
- [4] J. G. Checkelsky, R. Yoshimi, A. Tsukazaki, K. S. Takahashi, Y. Kozuka, J. Falson, M. Kawasaki, and Y. Tokura, Trajectory of the anomalous Hall effect towards the quantized state in a ferromagnetic topological insulator, Nat. Phys. 10, 731 (2014).
- [5] Y. Deng, Y. Yu, M. Z. Shi, Z. Guo, Z. Xu, J. Wang, X. H. Chen, and Y. Zhang, Quantum anomalous Hall effect in intrinsic magnetic topological insulator MnBi₂Te₄, Science 367, 895 (2020).
- [6] M. Serlin, C. L. Tschirhart, H. Polshyn, Y. Zhang, J. Zhu, K. Watanabe, T. Taniguchi, L. Balents, and A. F. Young, Intrinsic quantized anomalous Hall effect in a moiré heterostructure, Science 367, 900 (2020).
- [7] T. Li, S. Jiang, B. Shen, Y. Zhang, L. Li, T. Devakul, K. Watanabe, T. Taniguchi, L. Fu, and J. Shan, Quantum anomalous Hall effect from intertwined moiré bands, Nature 600, 641 (2021).
- [8] A. C. Mahoney, J. I. Colless, L. Peeters, S. J. Pauka, E. J. Fox, X. Kou, L. Pan, K. L. Wang, D. Goldhaber-Gordon,

- and D. J. Reilly, Zero-field edge plasmons in a magnetic topological insulator, Nat. Commun. **8**, 1836 (2017).
- [9] J. Wang, Q. Zhou, B. Lian, and S.-C. Zhang, Chiral topological superconductor and half-integer conductance plateau from quantum anomalous Hall plateau transition, Phys. Rev. B 92, 064520 (2015).
- [10] Q. L. He *et al.*, Chiral Majorana fermion modes in a quantum anomalous Hall insulator-superconductor structure, Science 357, 294 (2017).
- [11] M. Allen, Y. Cui, E. Yue Ma, M. Mogi, M. Kawamura, I. C. Fulga, D. Goldhaber-Gordon, Y. Tokura, and Z.-X. Shen, Visualization of an axion insulating state at the transition between 2 chiral quantum anomalous Hall states, Proc. Natl. Acad. Sci. U.S.A. 116, 14511 (2019).
- [12] M. Mogi, R. Yoshimi, A. Tsukazaki, K. Yasuda, Y. Kozuka, K. S. Takahashi, M. Kawasaki, and Y. Tokura, Magnetic modulation doping in topological insulators toward highertemperature quantum anomalous Hall effect, Appl. Phys. Lett. 107, 182401 (2015).
- [13] L. Pan, X. Liu, Q. L. He, A. Stern, G. Yin, X. Che, Q. Shao, P. Zhang, P. Deng, C.-Y. Yang, B. Casas, E. S. Choi, J. Xia, X. Kou, and K. L. Wang, Probing the low-temperature limit of the quantum anomalous Hall effect, Sci. Adv. 6, eaaz3595 (2020).
- [14] See Supplemental Material at http://link.aps.org/supplemental/ 10.1103/PhysRevLett.128.217704 for material synthesis and device fabrication, additional data from another set of devices, Hall matrix conversion, estimation of average 2D puddle sizes, and reproducibility of fluctuations.
- [15] I. T. Rosen, C. J. Trimble, M. P. Andersen, E. Mikheev, Y. Li, Y. Liu, L. Tai, P. Zhang, K. L. Wang, and Y. Cui, Fractional AC Josephson effect in a topological insulator proximitized by a self-formed superconductor, arXiv:2110.01039.
- [16] J. Weis and K. von Klitzing, Metrology and microscopic picture of the integer quantum Hall effect, Phil. Trans. R. Soc. A 369, 3954 (2011).
- [17] T. Patlatiuk, C. P. Scheller, D. Hill, Y. Tserkovnyak, G. Barak, A. Yacoby, L. N. Pfeiffer, K. W. West, and D. M. Zumbühl, Evolution of the quantum Hall bulk spectrum into chiral edge states, Nat. Commun. 9, 3692 (2018).
- [18] A. Yacoby, T. A. Fulton, H. F. Hess, L. N. Pfeiffer, and K. W. West, Compressibility images of the quantum Hall state, Physica E (Amsterdam) 9, 40 (2001).
- [19] K. Panos, R. R. Gerhardts, J. Weis, and K. von Klitzing, Current distribution and Hall potential landscape towards breakdown of the quantum Hall effect: A scanning force microscopy investigation, New J. Phys. 16, 113071 (2014).
- [20] P. Haremski, M. Mausser, A. Gauß, K. von Klitzing, and J. Weis, Electrically induced breakdown of the quantum Hall effect at different Hall bar widths: Visualizing the edge- and bulk-dominated regimes within a quantum Hall plateau, Phys. Rev. B 102, 205306 (2020).
- [21] L. Eaves and F. W. Sheard, Size-dependent quantised breakdown of the dissipationless quantum Hall effect in narrow channels, Semicond. Sci. Technol. 1, 346 (1986).

- [22] H. Doh and G. S. Jeon, Bifurcation of the edge-state width in a two-dimensional topological insulator, Phys. Rev. B 88, 245115 (2013).
- [23] B. Skinner, Coulomb disorder in three-dimensional Dirac systems, Phys. Rev. B 90, 060202 (2014).
- [24] M. Büttiker, Absence of backscattering in the quantum Hall effect in multiprobe conductors, Phys. Rev. B 38, 9375 (1988).
- [25] G. Lippertz, A. Bliesener, A. Uday, L. Pereira, A. A. Taskin, and Y. Ando, Current-induced breakdown of the quantum anomalous Hall effect, arXiv:2108.02081.
- [26] P. Weitz, E. Ahlswede, J. Weis, K. Klitzing, and K. Eberl, Hall-potential investigations under quantum Hall conditions using scanning force microscopy, Physica E (Amsterdam) 6, 247 (2000).
- [27] J. Weis, Hall potential profiles in quantum Hall samples measured by a low-temperature scanning force microscope, Int. J. Mod. Phys. B 21, 1297 (2007).
- [28] G. Timp, A. M. Chang, P. Mankiewich, R. Behringer, J. E. Cunningham, T. Y. Chang, and R. E. Howard, Quantum Transport in an Electron-Wave Guide, Phys. Rev. Lett. 59, 732 (1987).
- [29] J. K. Jain and S. A. Kivelson, Quantum Hall Effect in Quasi One-Dimensional Systems: Resistance Fluctuations and Breakdown, Phys. Rev. Lett. 60, 1542 (1988).
- [30] J. A. Simmons, H. P. Wei, L. W. Engel, D. C. Tsui, and M. Shayegan, Resistance Fluctuations in Narrow AlGaAs/GaAs Heterostructures: Direct Evidence of Fractional Charge in the Fractional Quantum Hall Effect, Phys. Rev. Lett. 63, 1731 (1989).
- [31] P. C. Main, A. K. Geim, H. A. Carmona, C. V. Brown, T. J. Foster, R. Taboryski, and P. E. Lindelof, Resistance fluctuations in the quantum Hall regime, Phys. Rev. B **50**, 4450 (1994).
- [32] A. M. Chang, G. Timp, T. Y. Chang, J. E. Cunningham, P. M. Mankiewich, R. E. Behringer, and R. E. Howard, Deviation of the quantum Hall effect from exact quantization in narrow GaAs-Al_xGa_{1-x}As heterostructure devices, Solid State Commun. **67**, 769 (1988).
- [33] E. O. Lachman, M. Mogi, J. Sarkar, A. Uri, K. Bagani, Y. Anahory, Y. Myasoedov, M. E. Huber, A. Tsukazaki, M. Kawasaki, Y. Tokura, and E. Zeldov, Observation of superparamagnetism in coexistence with quantum anomalous Hall $C = \pm 1$ and C = 0 Chern states, npj Quantum Mater. **2**, 70 (2017).
- [34] W. Wang, Y. Ou, C. Liu, Y. Wang, K. He, Q.-K. Xue, and W. Wu, Direct evidence of ferromagnetism in a quantum anomalous Hall system, Nat. Phys. **14**, 791 (2018).
- [35] E. O. Lachman, A. F. Young, A. Richardella, J. Cuppens, H. R. Naren, Y. Anahory, A. Y. Meltzer, A. Kandala, S. Kempinger, Y. Myasoedov, M. E. Huber, N. Samarth, and E. Zeldov, Visualization of superparamagnetic dynamics in magnetic topological insulators, Sci. Adv. 1, e1500740 (2015).